Insights on Na_3PS_4 solid-state electrolyte dry films: Interfacial stability and dry room compatibility

Dapeng Xu[a], *Wei Tang*[b*], *Feng Li*[b], *Ke Zhou*[b], *Junlin Wu*[c], *Alexander Fuqua*[b], *Yu-ting Chen*[c], *Dong Ju Lee*[b], *Jianting Qin*[a], *Andrea R. Tao*[b,c], *Ping Liu*[a,b,c], *Zheng Chen*[a,b,c,d*]

[a]Program of Chemical Engineering, University of California, San Diego, La Jolla, CA 92093, United States

[b]Department of NanoEngineering, University of California, San Diego, La Jolla, CA 92093, United States

[c]Program of Materials Science and Engineering, University of California, San Diego, La Jolla, CA 92093, United States

[d]Sustainable Power and Energy Center, University of California, San Diego, La Jolla, CA 92093, United States

AUTHOR INFORMATION

Corresponding to zhc199@ucsd.edu (Z. C.), wet003@ucsd.edu (W. T.)

ABSTRACT

The state-of-the-art pellet type sodium solid-state batteries (NaSSBs) suffer from inadequate humidity stability and poor mechanical properties, resulting in nonnegligible ohmic losses, limited crucial current density, and low energy density. To address these challenges, a dry process was proposed to fabricate Na_3PS_4 (NPS) film with only 0.2 wt.% polytetrafluoroethylene (PTFE) binders. The DFT results revealed that PTFE with hydrophobic groups improves moisture stability by reducing the available adsorption sites for H_2O on the surface. Furthermore, NaSSBs comprising NPS film and $NaCrO_2$ (NCO) cathode exhibited a high specific discharge capacity of 119.6 mAh·g^{-1} with an initial Coulombic efficiency (ICE) of 99.33%. After 24-hour exposure of NPS film to a dry room (RH, 0.1%), a high conductivity retention of 90% and stable cycling can be achieved for 100 cycles with a capacity retention of 83.5%, representing a significant advancement towards scaling up and practical application of NaSSBs.

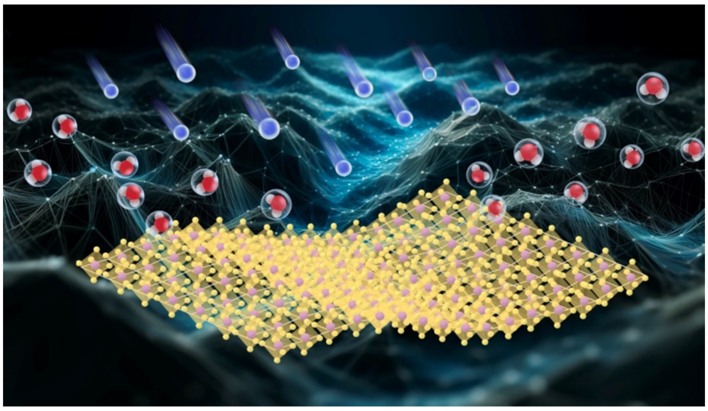

NaSSBs have gained attention as a promising technology for large-scale energy storage, which offers various advantages over conventional alkali metal ion batteries with flammable organic electrolytes, including intrinsic safety, high volumetric energy density, and cost-effectiveness[1–4]. Initially, pellet-type NaSSBs were demonstrated to have reasonable electrochemical performance based on advanced sulfide electrolytes[5]. However, the progress of the application of the sulfide electrolytes in developing competitive NaSSBs was hindered by their low ionic conductivity, air and moisture instability, ohmic losses, and sluggish Na^+ migration kinetics in ultrathick pellet-type NaSSBs. These issues limited the overall energy density, resulting in cell failure after long cycling[6–8]. Reducing the thickness of the SSE layer and improving the anti-moisture stability is crucial to address these challenges. These improvements are essential to realize the practical applications of NaSSBs.

The scalable production process is critical in driving the broad implementation and industrialization of highly competitive SSBs[9]. Various manufacturing techniques have been investigated, such as atomic layer deposition (ALD)[10], solvent-assisted casting[11,12], and dry-film (DF) processing[13,14]. The DF process has been recognized as the most promising approach among these methods to be applied in large-scale production at low cost. The ALD method alternately introduces a small amount of precursor gases to react on the substrate surface to form a film. It is suitable for precisely controlling film thickness and composition. However, the ALD process comes with high environmental and equipment standards and production costs; it is ideal for nano-coating on functional devices[15]. Solvent-assisted casting utilizes solvents to form films in a liquid environment but suffers from quality control and extra energy cost[16,17]. The sulfide electrolyte NPS, which is extremely sensitive and prone to degradation in moisture conditions, is primarily synthesized through a solid-state reaction via ball milling. Electrolyte films produced using this liquid-phase method have significantly reduced ionic conductivity and difficult quality control. DF processing stands out for its simplicity, speed, and cost-effectiveness, which is suitable for mass production and compatible with industrial applications. It allows for a broader film thickness range, helping to balance the trade-offs between energy density and the mechanical stability needed to prevent dendrite growth and extend cycle life in SSBs.[18,19]. For example, incorporating deformable sulfides allows for a thin yet durable film, even with a small quantity of inactive PTFE binder. This approach ensures that the overall ionic conductivity is not compromised by adjusting the PTFE loading ratio, fiberization temperature, calendar loop, and fiberization direction[20]. Recently, Zhang et al. presented a highly flexible $Li_{5.4}PS_{4.4}Cl_{1.6}$ film with a thickness of approximately 30 μm[21]. This film exhibited superionic conductivity of up to 8.4 $mS \cdot cm^{-1}$ at room temperature, comparable to organic electrolytes. He et al. reported DF processing of air-stable Na_3SbS_4 under atmospheric conditions[22]. This work addresses the limitations of traditional SSEs, such as their susceptibility to moisture and organic solvents, by fabricating thin, high-performance films in air. However, it should also be pointed out that the investigation into the influence of the PTFE ratio on the performance of SSE films and the discussion of the interface phenomenon is missing from this work. Further study is needed on the chemical and electrochemical stability of SSE films at the interface between the anode and SSE films, as well as their cycling performance in half/full cells.

Recent dry-processed research endeavors have predominantly concentrated on developing LiSSBs with considerable progress[23]. There has yet to be a suggestion or investigation on utilizing similar methods for NaSSBs. This gap in exploration presents a noteworthy research opportunity to discuss the potential of dry-processing-based NaSSBs and to reveal general instructive principles regarding process-performance relations. In this context, it is vital to incorporate advanced sulfides and dry processes to establish competitive NaSSBs. Specifically, the key to successful dry processing is a comprehensive understanding of PTFE binder-component interactions. Assessing the feasibility of dry-process NaSSBs requires considering the dry-process film's ionic conductivity, mechanical properties, and humidity stability. However, there is still a lack of systematic understanding regarding the sulfides to PTFE ratio and process parameters, which are closely associated with these indicators. Additionally, previous studies demonstrated that PTFE can be reduced to produce highly conductive carbon at a low potential, leading to current leakage and short-circuit issues in batteries[24,25]. Since sodium (-2.71V vs. standard hydrogen electrode, or SHE.) and sodium-tin alloy anodes (-2.4 to -2.1V vs. SHE.) possess an intrinsic low redox potential to the SHE[26], it is necessary to examine the suitability of the PTFE binder for sodium battery systems[27,28]. Moreover, despite extensive research on dry films, primarily focusing on film quality evaluation at the battery performance level, there remains a lack of information about in-depth systematic investigation into the interfacial phenomenon between the electrolyte film and the electrodes[21,29].

Herein, we introduce the inaugural study of a dry-processed sulfide film incorporating PTFE binders, systematically elucidating the interactions between these components. We investigated the PTFE tolerance and its effects on the ionic conductivity of NPS films from a low percentage of 0.2% to a high ratio of 5%. The interfacial phenomenon of NPS films was examined to study the reduction products of PTFE and the degradation mechanisms of ionic and electronic conductivity due to the interfacial reactions. A comparison between films and pellets was also conducted, showing higher CCD stability without short-circuiting from the NPS film. Due to industrial production being conducted in dry rooms, we also investigated the humidity stability and dry room compatibility of NPS films. With careful material characterization, the degradation mechanism of NPS was further revealed to be a reversible hydration reaction that happened at the beginning and, subsequently, a hydrolysis reaction causing irreversible ionic conductivity loss. For the dry room stability of NPS, we uncovered the relationship between conductivity decay and exposure time by comparing ionic conductivity and cycling stability of NPS film and pellet. Cells with the pristine and 24h-exposed dry-processed film with $NaCrO_2$ (NCO) as cathode and excess Na_9Sn_4 as anode exhibit a reversible capacity of 119.6 $mAh\cdot g^{-1}$ and 110.4 $mAh\cdot g^{-1}$, respectively, with a capacity retention of 88% and 83% at 0.2 C at an area capacity of 1 $mAh\cdot cm^{-2}$. This performance surpasses pellet-type batteries, emphasizing the advantages of utilizing dry-processed film electrolytes. Moreover, we compared the stability between the NPS and LPSCl films, which shows a drastic difference in electrochemical stability despite their similar trend in improving air stability by incorporating PTFE. The present study significantly contributes to a comprehensive understanding of feasibility, compatibility, interfacial stability, and moisture resistance in the dry fabrication process, advancing the field of NaSSB development.

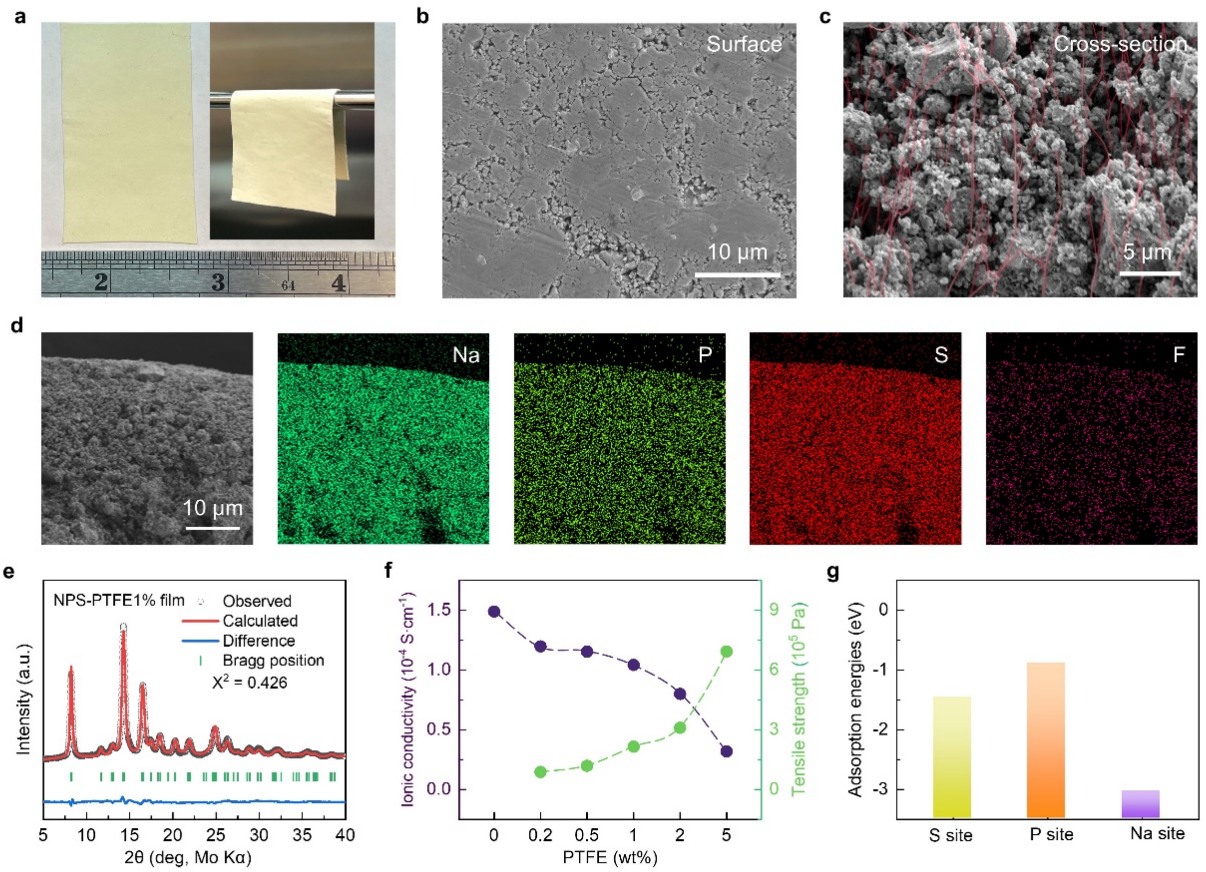

Figure 1. The fabrication of the NPS films and their physical properties. (a) The digital photo of fabricated SSE film with PTFE from the top side and bending appearance shows good mechanical properties. SEM images of the SSE dry film from the (b) surface and (c) cross-section side. The PTFE fibers are dyed into pink to increase their visibility. (d) EDX mapping of sodium, phosphorus, sulfur, and fluoride elements across the thickness of the NPS films. (e) Rietveld refinement of the XRD pattern of a representative SSE film. (f) The NPS films' ionic conductivity and tensile strength with different %PTFE. (g) Computed adsorption energies of PTFE onto the S, P, and Na sites of NPS.

Film characterization

NPS films were prepared using the dry process and incorporated PTFE binder with different weight percentages (wt.%) of 0.2%, 0.5%, 1%, 2%, and 5%. After the thickness was regulated to approximately 125 μm, NPS films showed a smooth surface with good mechanical properties, which can be bent without cracking or breaking (Fig.1a). Scanning electron microscopy (SEM) was used to examine the morphology of the film from surface and cross-section direction (Fig.1b, c). The PTFE fibers tangling with the NPS particles distributed within the NPS films can be observed under high magnification. Energy-dispersive X-ray spectroscopy (EDS) mapping was conducted to validate the uniform distribution of the NPS particles and PTFE network within the electrolyte substrate (Fig.1d). X-ray diffraction (XRD) was used to analyze the composition of the NPS film. The XRD Rietveld refinement can be indexed to the tetragonal phase NPS (PDF #00-048-1271) with no prominent PTFE peak (Fig. S1) detected from 1% PTFE film (Fig. 1e) due to the detection limit. The pattern parameters of the NPS from Rietveld refinement results are shown in Table S1. Compared with pristine NPS, the crystal parameters have negligible change.

Increasing the proportion of PTFE binder in the electrolyte improved the film's malleability and mechanical strength[30]. As shown in Fig. 1f, the tensile strength of the NPS films rose from 88.04 kPa of 0.2% PTFE film to 693.36 kPa of 5% PTFE film. The good mechanical properties were quantitatively demonstrated by this test, which benefit the resistance to the sodium dendrite growth during the cycling and extend the life of the cells. However, this came with a trade-off: the intertwined non-conductive PTFE fibers distributed in the NPS particles created physical barriers that obstructed ion transfer, decreasing Na^+ conductivity (σ_{Na+}). To illustrate, the σ_{Na+} of the NPS powder is 1.49×10^{-4} S·cm^{-1}. At the same time, NPS dry film with 0.2%, 0.5%, 1%, 2%, and 5% PTFE were recorded as 1.20×10^{-4},

1.15×10^{-4}, 1.04×10^{-4}, 8×10^{-5}, and 3.18×10^{-5} S·cm^{-1}, respectively (Fig.1f). By using the density functional theory (DFT) simulations, the interaction between the NPS and PTFE fibers (modeled as n-C_7F_{16}) was evaluated (Fig. S2, 3). Fig. 1g shows the adsorption energies for the adhesive effects between PTFE (n-C_7F_{16}) and different sites of NPS crystal structure. The strong adhesion occurring at the sodium sites simultaneously hinders the diffusion of the Na^+ and further decreases the ionic conductivity. However, as discussed in the later section, it can act as a protective agent to prevent hydrolysis for the NPS film.

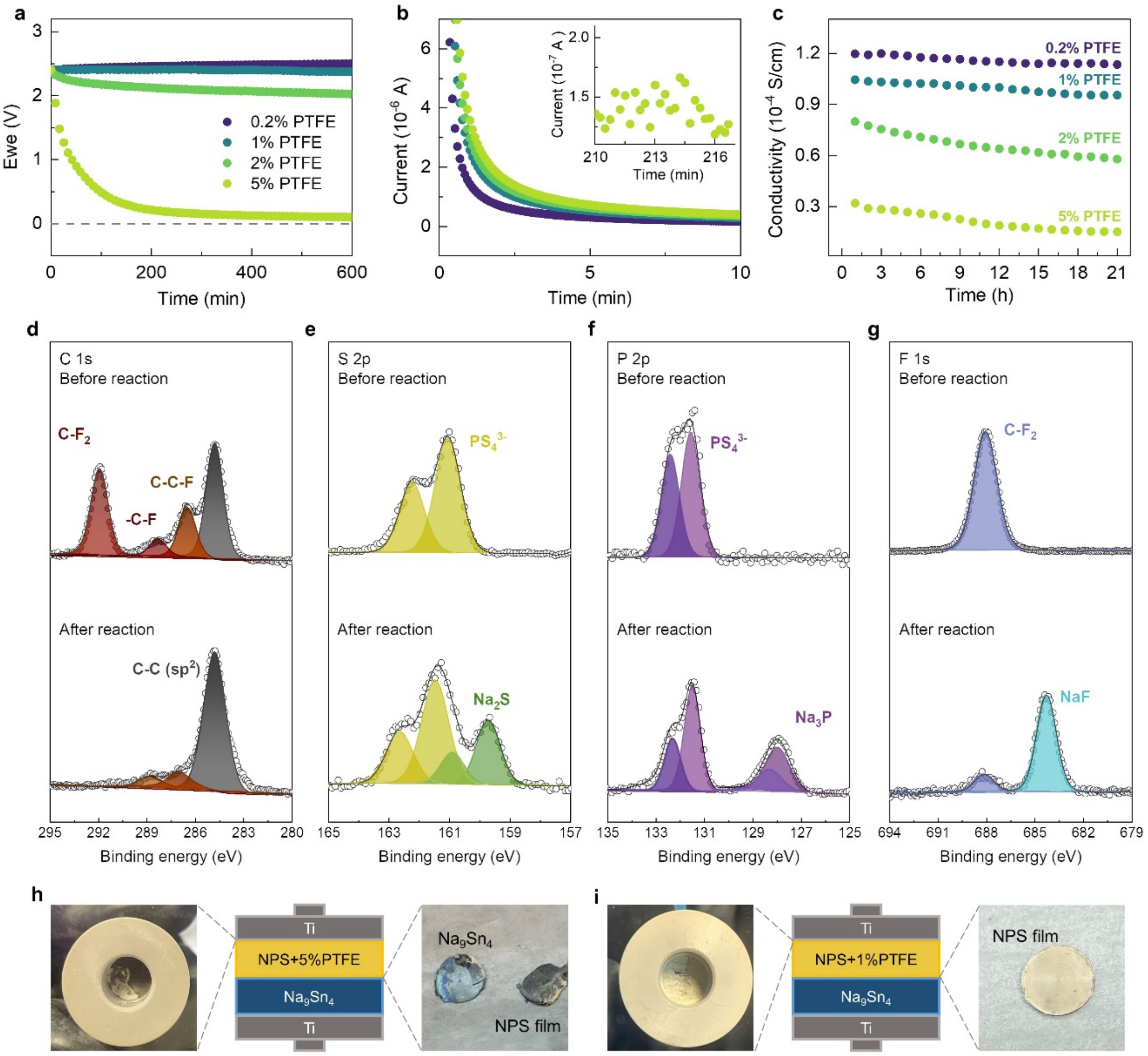

Figure 2. Chemical stability of the NPS films with 0.2%, 1%, 2%, and 5% PTFE ratio, tested

as a configuration of NPS film||Na_9Sn_4. (a) The OCV evolution of NPS films in 10 hours; (b) DC polarization to determine the electronic conductivity under 1V bias; (c) Comparison of the attenuation of ionic conductivity of the NPS film with different %PTFE; (d, e, f, g) XPS characterization of 5% PTFE films before and after the reaction with Na_9Sn_4 anode: C 1s, S 2p, P 2p and F 1s binding energy regions of the spectrum; (h, i) The photos of the NPS films with 5% and 1% PTFE to reveal the changes after reaction directly.

Chemical and electrochemical stabilities

The chemical and electrochemical stability of NPS films contacted with sodium-tin alloy (Na_9Sn_4 was selected since its high Na^+ diffusion kinetics that lead to better galvanostatic cycling stability[26,31]) were comprehensively investigated. The open-circuit voltage (OCV) evolution and electrochemical impedance spectroscopy (EIS) were used to reveal the chemical stability between the NPS films with different PTFE weight percentages (5%, 2%, 1%, and 0.2%) and Na_9Sn_4 anode. For the 5% PTFE film, the OCV fell to 0 V within 3h (Fig. 2a), indicating the cell was internally short-circuited. The electronic conductivity showed noticeable fluctuation in the late period of the test (Fig. 2b). Other cells with PTFE content lower than 2% showed stable OCV, suggesting NPS films at lower PTFE ratio films (0.2% to 2%) did not suffer a reaction that changed the electronic conductivity seriously when contacted with Na_9Sn_4. Over a continuous testing period of 24h, σ_{e-} remained stable at 3.049×10^{-9} $S\cdot cm^{-1}$, 2.781×10^{-9} $S\cdot cm^{-1}$, and 2.632×10^{-9} $S\cdot cm^{-1}$, for 2%, 1%, 0.2% PTFE films respectively. Despite higher PTFE content resulting in increased electronic conductivity, these films did not form an electronic conductive pathway penetrating the electrolyte layer and causing the short circuit[32]. Lastly, the σ_{Na+} degradation of NPS film from Na_9Sn_4 alloy contact was analyzed by EIS, as shown in Fig. 2c and S4. The σ_{Na+} of the 2% PTFE film experiences a reduction of approximately 28% (from 7.989×10^{-5} $S\cdot cm^{-1}$ to 5.788×10^{-5} $S\cdot cm^{-1}$) post 21h of interaction with the Na_9Sn_4 anode. The σ_{Na+} of 0.2% PTFE film slightly decreased from 1.2×10^{-4} $S\cdot cm^{-1}$ to

1.14×10^{-4} S·cm^{-1}, suggesting that low PTFE ratio enhances the interfacial stability of NPS film against Na_9Sn_4 anode. The EIS plots describing the impedance evolution of the interfacial reaction between the NPS film (0.2% or 2% PTFE) and the Na_9Sn_4 anode are shown in Fig. S5 a,b. After 20 hours, the impedance of the cell with 2% PTFE film shows a drastic increase, while the impedance of the cell with 0.2% PTFE film does not change significantly. The equivalent circuit fitting was performed using the data at 0h and 20h for the 2% PTFE film cell, with the results shown in Fig. S5c, d. At 0h, the EIS curve reveals a resistance of about 387Ω in the high-frequency region, corresponding to the resistance of the pristine NPS film. After 20h of contact with the anode, the resistance of the NPS film increased to 438Ω, indicating that a reaction occurred between NPS and the sodium-tin alloy, leading to a decrease in its ionic conductivity. Simultaneously, a new semicircle appeared in the mid to low-frequency region, corresponding to an interfacial resistance of 492.6Ω between the anode and the electrolyte, suggesting that PTFE was reduced after contact and resulted in the formation of SEI, which increased the overall impedance of the cell.

To study the NPS film || Na_9Sn_4 interfacial reaction and its products, the 5% PTFE film after the reduction was disassembled from the anode for X-ray photoelectron spectroscopy (XPS) analysis. As shown in Fig. 2d, the C 1s spectrum exhibits a significant decrease in the peak intensity of the C-F (288.32 eV), C-C-F (286.51 eV), as well as the $C\text{-}F_2$ (291.94 eV) relating to the defluorination process of PTFE. Also, the increased signal intensity with the binding energy of 284.8 eV indicates the formation of electronic conductive sp^2 carbon as a product. Additionally, a comparison of the FTIR spectrum between the pristine PTFE and its reduced product is shown in Fig. S6. The formation of the C=C bonds is clearly observed, supporting the existence of such products, which caused a severe shorting penetrating the whole electrolyte layer, as shown in the OCV evolution test[20]. Fig. 2e reveals that Na_2S in the S 2p peak position[33] (161.8 eV) is one of the products of NPS after being reduced by Na_9Sn_4 alloy. From the P 2p spectrum (Fig. 2f), the reduction in PS_4^{3-} intensity also reflects the degradation of NPS; Accordingly, the characteristic peak of Na_3P (127.9eV)[8] indicates another decomposition product besides Na_2S. Insulating NaF shown in the F 1s peak position[34] (684.5 eV) was confirmed as the other side-product from PTFE reduction (Fig. 2g). The XPS results demonstrate that PTFE in the electrolyte films suffered reduction (Eq. 1) and permeated the entire electrolyte layer at a high content (5%), appearing as black products (Fig. 2h) on both the anode and cathode sides after the reaction. Nevertheless, the films are relatively stable at < 2% of PTFE (Fig. 2i). Besides PTFE being reduced by contacting Na_9Sn_4, NPS also undergoes decomposition on the anode side, which is confirmed by the sodium sulfide (Na_2S) and sodium phosphide (Na_3P) being generated on the interface between the NPS electrolyte and the Na_9Sn_4 anode, attributing to the decrease of σ_{Na+} in all NPS films[35,36]. Based on the XPS analysis, the decomposition reaction of NPS film when contacted with Na_9Sn_4 can be described in reaction (Eq. 2).

$$(\mathrm{C_2F_4})_n + 4n\ \mathrm{Na} \rightarrow 4n\ \mathrm{NaF} + 2n\ \mathrm{C}\ (\mathrm{sp}^2) \tag{1}$$

$$\mathrm{Na_3PS_4} + 8\ \mathrm{Na} \rightarrow 4\ \mathrm{Na_2S} + \mathrm{Na_3P} \tag{2}$$

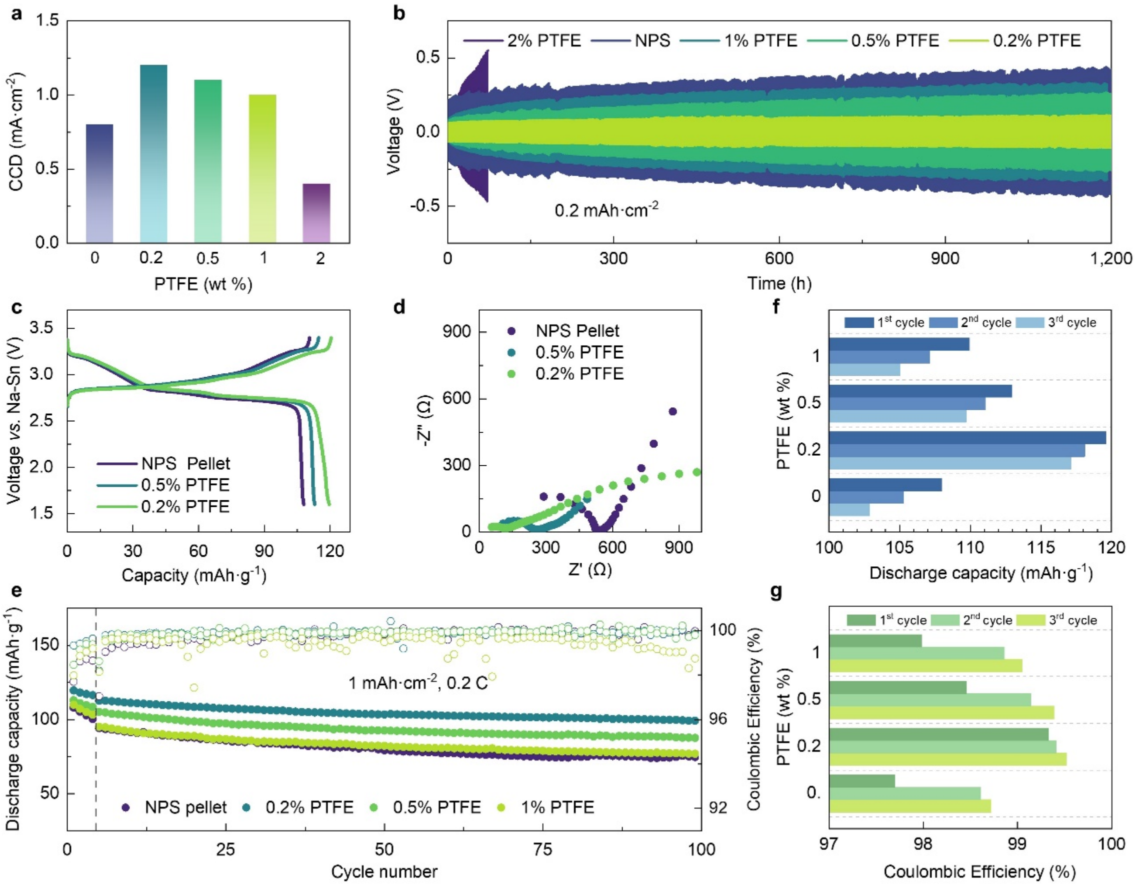

Figure. 3 Electrochemical stabilities characterized by CCD test and cell performance of the NPS films. (a) The trend of the CCD for NPS pellet and films with 0.2%, 0.5%, 1%, and 2% PTFE ratio without soft shorting; (b) Symmetric cell plating and stripping at 0.2 mA/cm^2; Cell performance of the film cells tested as NCO||NPS film (or pellet)||Na$_9$Sn$_4$ cell configuration; (c) Voltage profile as a function of specific capacity for the 1st cycle; (d) EIS of the NPS pellet or film cells before cycling; (e) Long-term cycling performance of the NPS pellet or film cell; (f, g) Comparison of the first three-cycle specific discharge capacity and CE of the half cells.

Critical current density (CCD) tests for symmetric Na$_9$Sn$_4$||NPS film||Na$_9$Sn$_4$ cells were conducted to evaluate the electrochemical stability of NPS films. NPS pellet exhibits a CCD of 0.8 mA·cm^{-2}, as shown in Fig. S7, similar to the previous report[37]. The 1% PTFE film began to show a soft short circuit, a condition where there is a partial path of dendrites that does not immediately lead to a full short circuit, when the current density exceeded 1.0 mA/cm² (Fig. 3a), indicating the current leakage and the risk of decreasing the Coulombic efficiency[20]. A similar trend was observed with the 0.5% and 0.2% films, which displayed soft shorting at current densities of 1.1 mA·cm^{-2} and 1.2 mA·cm^{-2}, respectively. However, 2% PTFE film can only sustain a CCD of 0.4 mA·cm^{-2}. The trend of the CCD for NPS powder and films without soft shorting shows a clear improvement when employing NPS film with a PTFE ratio lower than 1%.

To assess the cycling stability during sodium plating/stripping, symmetrical cells were assembled and tested at a current density of 0.2 mA·cm^{-2}. As the cycling progressed, the voltage profile indicating the ohmic response began to rise, suggesting an increase in cell impedance by forming the passivation layer[38]. After about 1200h of operation, a voltage difference of 91.5 mV between the 0.2% and 0.5% films was observed despite their nearly identical voltages at the start of cycling (Fig. 3b). In comparison, the cell constructed with NPS powder showed a rate of impedance increase similar to that observed for the 1% PTFE film. The cell with 2% PTFE suffered a significant increase in voltage, and the soft shorting appeared after 70 cycles. The cycling performance of the NPS films with a PTFE ratio lower than 1% is better than that of the NPS powder, which can be attributed to the lower achievable thickness using the dry film process. For a pellet cell, at least 70 mg NPS must be added to serve as a support layer to avoid cracks and being broken, which is around 400 μm thick. But for a film cell, since the thickness of the NPS film is only around 120 μm, it reduces the impedance by 70%. In addition, the smoother surface of the SSE layer without cracks obtained by the dry film method benefits the ionic conduction pathways at the interface and reduces the interface resistance[13,39]. This advantage is particularly noticeable when the PTFE content is decreased to 0.2%, with limited influence from PTFE, which shows minimal change on overpotential for 1200 h operation.

NCO || NPS film || Na_9Sn_4 cells were assembled to evaluate the cycling performance of the electrolyte films with different PTFE ratios. For comparison, the discharge capacity and Coulombic efficiency (CE) of the NPS powder cell were assessed as a control, and cells with 0.2-2% PTFE film were loaded with the same cathode active material (8.3 mg·cm^{-2} NCO, about 1 mAh·cm^{-2}). All batteries were tested at 40 °C, starting with four formation cycles at C/10 and then cycled at C/5. Fig. 3c reveals that the specific discharge capacity of the first cycle decreases with higher PTFE content: 120 mAh·g^{-1}, 113 mAh·g^{-1}, and 110 mAh·g^{-1} for electrolyte with PTFE contents at 0.2%, 0.5%, and 1%, respectively. Cells with NPS pellet electrolyte exhibit a specific discharge capacity of 108 mAh·g^{-1}, slightly lower than the 1% PTFE cell. ICE of 0.2% PTFE film cell reached 99.33%, higher than the other pellet cells reported before[37]. The improved EC performance of the film cells can be attributed to the lower film thickness, facilitated Na^{+} transport, and reduced overpotential and ionic conductivity, which can be proved by EIS (Fig. 3d).

Cyclic voltammetry (CV) was used to characterize the electrochemical reaction inside the battery at different voltages (Fig. S8). The oxidation/reduction peaks at 3.03V/2.6V and 3.3V/3.07V correspond to the Cr^{3+}/Cr^{4+} redox couple and the phase transformation of the NCO cathode. No extra peak related to the reaction of the PTFE at the low voltage region was detected, indicating the reduction of PTFE occurred only at the anode/electrolyte interface. After 100 cycles, the capacity retention of film cells was 88 %, 83%, and 81%, for 0.2%, 0.5%, and 1% PTFE film electrolyte, respectively, surpassing the 79 % retention of NPS pellet electrolyte (Fig. 3e). The NPS film prepared by the dry process can have up to 1% PTFE content in NCO || NPS film || Na_9Sn_4 system without reducing the cycle performance and causing failure. While a higher content of PTFE improves the processability and mechanical properties of the electrolyte film, the higher risk of cell shorting makes it infeasible for full cell applications. Similar results were demonstrated when using a lower potential anode, $Na_{15}Sn_4$ (0.1V vs. Na/Na^+), instead of Na_9Sn_4 (0.3V vs. Na/Na^+)[26,37], which was depicted in Figure S9 and further discussed in the supporting information.

To better manifest the reduction behavior of PTFE at different anodic potentials, PTFE was pressed as a pellet and contacted with $Na_{15}Sn_4$ and sodium metal, and the interface was observed after being held at 1 MPa pressure for 10 minutes. As shown in Fig. S10, the sample in contact with sodium metal formed large amounts of black products at the interface as a sticky interlayer, which is evenly distributed and has a specific thickness. Their adhesion to the sodium metal surface makes the PTFE layer challenging to separate, revealing a violent reaction. However, it was found that the PTFE layer in contact with the sodium-tin alloy is reduced more mildly than that of the sodium metal. As seen from Fig. S10f, no interlayer with a certain thickness was formed, and the surface of PTFE became darker with black products. It is easy to be separated into two complete pieces when disassembling. This test more intuitively proves that PTFE has different reducing properties under different anodic potentials.

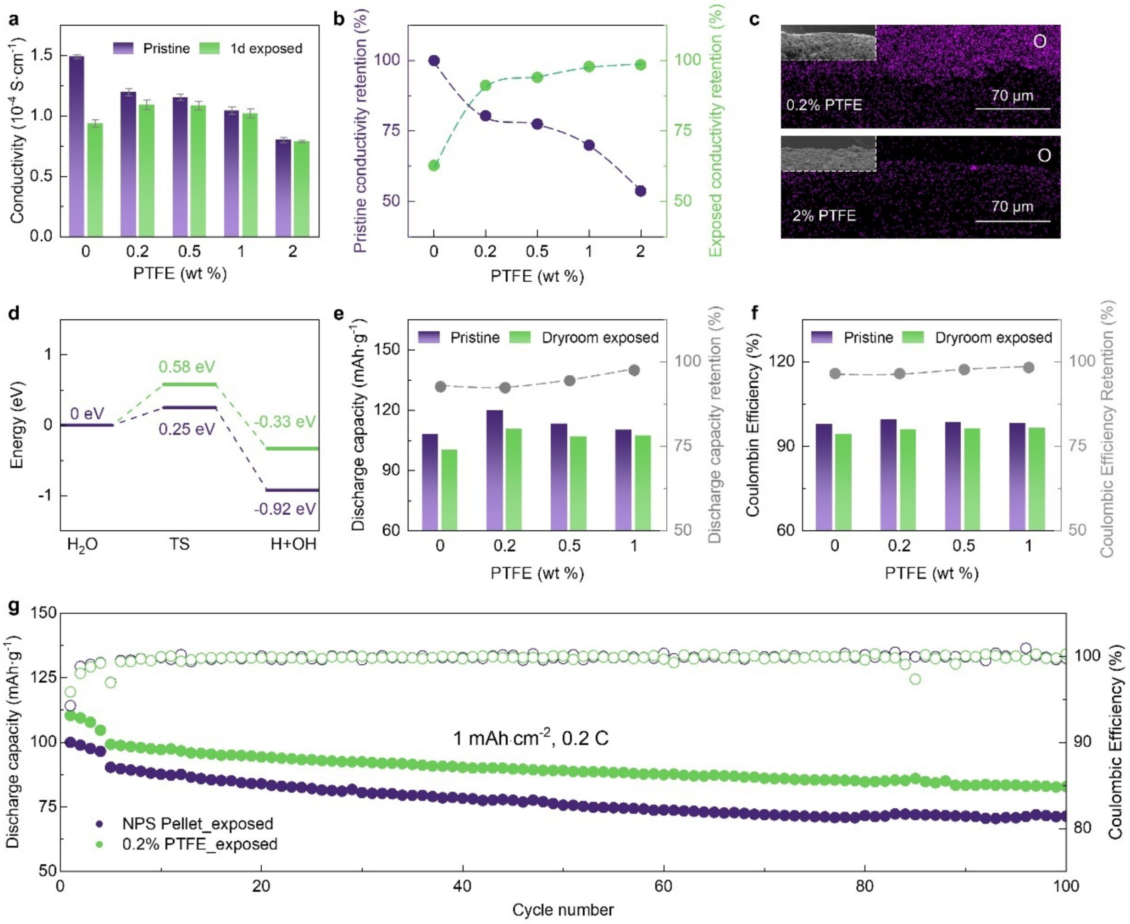

Figure 4. A comparison of the electrochemical properties and half-cell performance between NPS films with various PTFE ratios and pellets before and after exposure to the dry room. (a) The change of the ionic conductivity after exposure to the dry room for 24h; (b) The ratio of the residual ionic conductivity to the pristine value; (c) SEM images and EDS mapping of oxygen element distributed on the NPS films after exposure to show the extent of the degradation; (d) The hydrolysis energy barriers for NPS powder and NPS film (NPS@n-C_7F_{16}); Comparison between the pristine and exposed samples of the first cycle (e) discharge capacity and (f) CE; (g) Long-term cycling performance of the half-cell assembled with dry-room exposed NPS.

Moisture stability

Industrial battery production typically occurs in a dry room with low water content, reducing manufacturing costs compared to pure inert gas like argon[40]. Like most sulfide electrolytes, the NPS electrolyte exhibits a high sensitivity to water, rapidly deteriorating with moisture and resulting in a rapid decrease in ionic conductivity[41]. Fig. S11 compares the changes of σ_{Na+}

over time for NPS in ambient air (RH = 52%, T_{dew} = 12.7°C) and the dry room (RH = 0.1%, T_{dew} = -56°C). Initial exposure led to a rapid σ_{Na+} decrease: dry room samples dropped from 1.27×10^{-4} $S\cdot cm^{-1}$ to 5.54×10^{-5} $S\cdot cm^{-1}$ in 24 hours. Air-exposed samples were reduced to 4.7×10^{-7} $S\cdot cm^{-1}$ in the same period. The decline in σ_{Na+} almost completed at the onset of the exposure, especially for dry room conditions. XRD and XPS tests were carried out to characterize the chemical composition changes during exposure. The XRD profile (Fig. S12a) of the sample exposed to air for 24 hours exhibited multiple mixed peaks. After heating at 220°C for 5 hours to remove the absorbed/structured water, the peak distribution became similar to that of the NPS powder. XRD refinement was utilized to analyze the products further (Fig. S12b, Table S2). The solid byproduct formed during the exposure process was identified as Na_3POS_3, with a ratio of 37.91%. Notably, the samples exposed to the dry room exhibited no substantial alterations in their XRD patterns (Fig. S12c).

The XPS of S 2p and P 2p characterization of the three samples is depicted in Fig. S13. No new peaks were detected in the S 2p spectrum. Still, a progressive decline in the intensity of the PS_4^{3-} peak at 161.04eV indicates an irreversible sulfur loss due to H_2S release. In the P 2p spectrum, the POS_3^{3-} peak proves the O substitution of the S during the degradation, discernible at 132.66 eV. Compared to air-exposed samples, the signal intensity of dry room-exposed products was significantly lower. To elucidate the reaction pathway during the initial exposure phase, Fourier Transform Infrared (FTIR) and Raman spectroscopy with better sensitivity to water were employed to characterize the hydration and hydrolysis processes further. FTIR spectroscopy (Fig. S14a) revealed -OH peaks at 1627.63 cm^{-1} and 3312.63 cm^{-1} within two minutes of exposure, indicating the presence of absorbed water. Multiple peaks between 596.86

cm^{-1} and 1131.50 cm^{-1} are associated with POS_3^{3-} bonds but with a limited intensity[42,43]. In the Raman spectrum (Fig. S14b), four characteristic peaks of PS_4^{3-} decreased in intensity, accompanied by a discernible shift towards higher wavenumbers of the ν2 peaks. This shift signifies a contraction in atomic spacing and an escalation in molecular stress, indicative of modifications in the NPS crystal structure attributable to the incorporation of structure water.

Based on the above results (Fig. S11-12) and discussion, the degradation mechanism can be described as such a process: at the beginning of the degradation, the H_2O molecules adsorbed induce the formation of crystal water within the NPS, altering its crystal parameters, as a hydration process. This transformation impacts the transport of sodium ions, leading to a substantial reduction in ionic conductivity. However, such a process is reversible and can be recovered via heating. Next, chemical hydrolysis commences as the reaction advances and oxygen atoms start supplanting sulfur atoms permanently, triggering an irreversible performance deterioration. Such a reaction, accompanied by the liberation of H_2S gas, can be expressed by Eq. 3.

$$\mathrm{Na_3PS_4} + \mathrm{H_2O} \rightarrow \mathrm{Na_3POS_3} + \mathrm{H_2S}\uparrow \tag{3}$$

A series of tests were conducted to evaluate NPS film's compatibility under dry room conditions and reveal its humidity stability. NPS powder and NPS films with varying concentrations (0.2%, 0.5%, 1%, and 2%) of PTFE were exposed to the dry room maintained at a dew point of -56°C (RH 0.1%) for 24h. After the exposure, σ_{Na+} measurements revealed distinct behaviors between the NPS films and NPS powders (Fig. 4a). The NPS films maintained over 90% of their original σ_{Na+}. In contrast, the NPS powders exhibited an approximate 38% decrease (Fig. 4b). Since the hydration and hydrolysis of NPS can lead to the substitution of the sulfur by oxygen[44], the degree of degradation can be qualitatively assessed by comparing the degree of oxidation. Dispersive X-ray spectroscopy (EDS) was used to analyze the reaction depth in a cross-section area during exposure by measuring the intensity of the oxygen. In addition, NaOH was used to eliminate the interference from CO_2 in the atmosphere during the exposure in the humility-controlled chamber. When evaluating the oxygen distribution, the 0.2% PTFE film exhibited a more vigorous oxygen signal intensity than the 2% PTFE film, indicating a higher level of water absorption. Notably, a stronger oxygen signal was observed near the surface of the 2% PTFE membrane, suggesting that PTFE slows down moisture diffusion and hydrolysis in the film. This, in turn, results in less decay in conductivity (Fig. 4c). By calculating the activation energy barrier of electrolyte hydrolysis, it was determined that NPS films with PTFE are less prone to hydrolysis (Fig. 4d). This phenomenon can be attributed to the highly electronegative fluorine atoms connecting as C-F covalent bonds on the carbon backbone of PTFE, creating a hydrophobic local environment that enhances the air stability of the NPS films. The consequential limitation in available reaction sites for hydration and hydrolysis further contributed to higher residual σ_{Na+} of the films with more PTFE. To substantiate the hydrophobic protection effect of PTFE, we fabricated LPSCl films with 0.2% PTFE and compared their stability with NPS counterparts. These two SEs showed the same trend in the change of ionic conductivity (Fig. S15). Besides, the DFT calculation results (Fig. S15c) are similar to the NPS, indicating that PTFE fibers can inhibit electrolyte hydrolysis for the same reason.

After 24h of exposure in the dry room, the NPS film was assembled in half cells for the electrochemical performance test. The performance was then compared with their original values. After exposure, all NPS pellet and film cells delivered a slightly lower capacity and lower ICE (Fig. 4e, f). Specifically, the capacity of the NPS pellet cell receded from 108 mAh·g^{-1} to 100 mAh·g^{-1}. In contrast, the 1% PTFE film cell presented a modest reduction, from 110 mAh·g^{-1} to 107 mAh·g^{-1}. From the residual σ_{Na+} of the exposed films, the 1% and 0.5% PTFE films have approximately the same value, which is benefited from the higher PTFE ratio. The initial discharge capacity and the ICE suggest that films with a higher PTFE content experience a less pronounced performance decay than their initial values. The performance alterations in the 0.2% PTFE film cell were parallel to those observed in the pellet cell. These findings strongly corroborate the hypothesis that by providing a moisture isolation effect, PTFE enhances the air stability of the NPS films.

In conclusion, this study introduces an innovative NPS film electrolyte produced via a dry-process technique. It systematically examines the impact of PTFE ratios and their fundamental mechanisms in determining chemical, electrochemical, and moisture stability. The optimized NPS film exhibits exceptional flexibility and good ionic conductivity. Leveraging the minimized PTFE ratio and inherent hydrophobic properties, the films demonstrate outstanding electrochemical stability, compatibility with sodium-tin alloy anodes, and commendable moisture resistance, as affirmed by comprehensive characterizations and DFT simulation. Consequently, NaSSBs constructed using the NPS film showcase remarkable performance and superior discharge capacity compared to pellet cells and manifest a capacity retention rate of 88% over 100 cycles. Furthermore, a comprehensive comparison between NPS and LPSCl, the most widely used SSE material in LiSSBs, was conducted regarding PTFE tolerance, interfacial phenomenon, cycling stability, and dry room stability. Though Li SSE films have been well studied, it is important to recognize that Na SSE dry films exhibit distinct properties. Therefore, a direct translation of knowledge from Li counterparts to Na SSE dry films may not be applicable. To facilitate understanding, the relevant comparisons were summarized, and they are presented in Table S3. The sustained operational stability of NaSSBs, particularly in humid conditions, underscores the potential of such SSE films for practical manufacturing and widespread applications. This research addresses a critical gap in developing SSE based on chemical and air-sensitive materials, paving the way for the dry manufacturing of SSBs.

SUPPORTING INFORMATION

Experimental methods: Material synthesis; NPS film fabrication; Exposure; Materials characterization; Electrochemical characterization; Electrochemical performance; XRD pattern of the pure PTFE; The pattern parameters of the Rietveld refinement results; DFT calculations to the NPS and PTFE (n-C_7F_{16}) structures; The structures for adsorption energies of the PTFE n-C_7F_{16}; The Nyquist plot of NPS films with different PTFE ratios; The EIS plots of the impedance evolution of the interfacial reaction; FTIR spectrum of PTFE contacting sodium metal anode; The CCD test of the NPS pellet; CV curve of NPS pellet and 1% PTFE film cell; Photos of the PTFE contacted the sodium metal and sodium tin alloy; Ion conductivity degradation at different exposure times; XRD pattern of exposed NPS and refinement results; XPS of NPS before and after the exposure; In situ FTIR and Raman test of NPS during exposure to the air; The change of the ion conductivity of LPSCl films before and after exposure; A comparison of the properties of the NPS film and LPSCl film.

AUTHOR INFORMATION

Corresponding Author

Zheng Chen - Department of NanoEngineering, University of California San Diego, La Jolla, California 92093, United States; Program of Chemical Engineering, University of California, San Diego, Sustainable Power and Energy Center (SPEC), the University of California San Diego, La Jolla, California 92093, United States; Sustainable Power and Energy Center, University of California, San Diego, La Jolla, California 92093, United States; https://orcid.org/0000-0002-9186-4298;

Email: zhc199@ucsd.edu

Wei Tang - Department of NanoEngineering, University of California, San Diego, La Jolla, CA 92093, United States.

Email: wet003@ucsd.edu

Authors

Dapeng Xu - Program of Chemical Engineering, University of California, San Diego, La Jolla, CA 92093, United States.

Feng Li - Department of NanoEngineering, University of California, San Diego, La Jolla, CA 92093, United States.

Ke Zhou - Department of NanoEngineering, University of California, San Diego, La Jolla, CA 92093, United States

Junlin Wu - Program of Materials Science, University of California, San Diego, La Jolla, CA 92093, United States.

Alexander Fuqua - Department of NanoEngineering, University of California, San Diego, La Jolla, CA 92093, United States.

Yu-ting Chen - Program of Materials Science, University of California, San Diego, La Jolla, CA 92093, United States.

Dong Ju Lee - Department of NanoEngineering, University of California, San Diego, La Jolla, CA 92093, United States.

Jianting Qin - Program of Chemical Engineering, University of California, San Diego, La Jolla, CA 92093, United States.

Andrea R. Tao - Material Science and Engineering Program, University of California, San Diego, 9500 Gilman Drive, La Jolla, CA, 92093, United States. Department of NanoEngineering, University of California, San Diego, 9500 Gilman Drive, La Jolla, CA, 92093, United States.

Ping Liu - Program of Materials Science and Engineering, University of California San Diego, La Jolla, California 92093, United States; Department of Nanoengineering, University of California San Diego, La Jolla, California 92093, United States;

ACKNOWLEDGMENT

The National Science Foundation provided funding to support this work through the Future Manufacturing (FM) grant no. 2134764. This work was partly performed at the San Diego Nanotechnology Infrastructure (SDNI) of UCSD, a member of the National Nanotechnology Coordinated Infrastructure, supported by the National Science Foundation (grant ECCS-2025752). The authors acknowledge the use of facilities and instrumentation at the UC Irvine Materials Research Institute (IMRI), which is partly supported by the National Science Foundation through the UC Irvine Materials Research Science and Engineering Center (DMR-2011967). Specifically, the XPS work was performed using instrumentation funded in part by the National Science Foundation Major Research Instrumentation Program under grant no. CHE-1338173.

CONFLICTING INTERESTS

The authors declare no competing financial interest.

REFERENCES

(1) Hirsh, H. S.; Li, Y.; Tan, D. H. S.; Zhang, M.; Zhao, E.; Meng, Y. S. Sodium-Ion Batteries Paving the Way for Grid Energy Storage. *Adv. Energy Mater.* **2020**, *10* (32), 2001274. https://doi.org/10.1002/aenm.202001274.

(2) Zhou, W.; Li, Y.; Xin, S.; Goodenough, J. B. Rechargeable Sodium All-Solid-State Battery. *ACS Cent. Sci.* **2017**, *3* (1), 52–57. https://doi.org/10.1021/acscentsci.6b00321.

(3) Tarascon, J.-M. Na-Ion versus Li-Ion Batteries: Complementarity Rather than Competitiveness. *Joule* **2020**, *4* (8), 1616–1620. https://doi.org/10.1016/j.joule.2020.06.003.

(4) Cao, D.; Zhao, Y.; Sun, X.; Natan, A.; Wang, Y.; Xiang, P.; Wang, W.; Zhu, H. Processing Strategies to Improve Cell-Level Energy Density of Metal Sulfide Electrolyte-Based All-Solid-State Li Metal Batteries and Beyond. *ACS Energy Lett.* **2020**, *5* (11), 3468–3489. https://doi.org/10.1021/acsenergylett.0c01905.

(5) Lu, P.; Xia, Y.; Sun, G.; Wu, D.; Wu, S.; Yan, W.; Zhu, X.; Lu, J.; Niu, Q.; Shi, S.; Sha, Z.; Chen, L.; Li, H.; Wu, F. Realizing Long-Cycling All-Solid-State Li-In||TiS2 Batteries Using Li6+xMxAs1-XS5I (M=Si, Sn) Sulfide Solid Electrolytes. *Nat. Commun.* **2023**, *14* (1), 4077. https://doi.org/10.1038/s41467-023-39686-w.

(6) Lou, S.; Zhang, F.; Fu, C.; Chen, M.; Ma, Y.; Yin, G.; Wang, J. Interface Issues and Challenges in All-Solid-State Batteries: Lithium, Sodium, and Beyond. *Adv. Mater.* **2021**, *33* (6), 2000721. https://doi.org/10.1002/adma.202000721.

(7) Hou, W.; Guo, X.; Shen, X.; Amine, K.; Yu, H.; Lu, J. Solid Electrolytes and Interfaces in All-Solid-State Sodium Batteries: Progress and Perspective. *Nano Energy* **2018**, *52*, 279–291. https://doi.org/10.1016/j.nanoen.2018.07.036.

(8) Deysher, G.; Chen, Y.-T.; Sayahpour, B.; Lin, S. W.-H.; Ham, S.-Y.; Ridley, P.; Cronk, A.; Wu, E. A.; Tan, D. H. S.; Doux, J.-M.; Oh, J. A. S.; Jang, J.; Nguyen, L. H. B.; Meng, Y. S. Evaluating Electrolyte–Anode Interface Stability in Sodium All-Solid-State Batteries. *ACS Appl. Mater. Interfaces* **2022**, *14* (42), 47706–47715. https://doi.org/10.1021/acsami.2c12759.

(9) Singer, C.; Schnell, J.; Reinhart, G. Scalable Processing Routes for the Production of All-Solid-State Batteries—Modeling Interdependencies of Product and Process. *Energy Technol.* **2021**, *9* (1). https://doi.org/10.1002/ente.202000665.

(10) Wang, B.; Bates, J. B.; Hart, F. X.; Sales, B. C.; Zuhr, R. A.; Robertson, J. D. Characterization of Thin-Film Rechargeable Lithium Batteries with Lithium Cobalt Oxide

Cathodes. *J. Electrochem. Soc.* **1996**, *143* (10), 3203–3213. https://doi.org/10.1149/1.1837188.

(11) Ji, W.; Zhang, X.; Qu, H.; Xin, L.; Luedtke, A. T.; Huang, H.; Lambert, T. H.; Qu, D. Polyimide as a Durable Cathode for All-Solid-State Li(Na)−organic Batteries with Boosted Cell-Level Energy Density. *Nano Energy* **2022**, *96*, 107130. https://doi.org/10.1016/j.nanoen.2022.107130.

(12) Lee, D.; Lee, H.; Song, T.; Paik, U. Toward High Rate Performance Solid-State Batteries. *Adv. Energy Mater.* **2022**, *12* (27). https://doi.org/10.1002/aenm.202200948.

(13) Shin, D.; Nam, J. S.; Nguyen, C. T. L.; Jo, Y.; Lee, K.; Hwang, S. M.; Kim, Y.-J. Design of Densified Nickel-Rich Layered Composite Cathode via the Dry-Film Process for Sulfide-Based Solid-State Batteries. *J. Mater. Chem. A* **2022**, *10* (43), 23222–23231. https://doi.org/10.1039/d2ta05021h.

(14) Hippauf, F.; Schumm, B.; Doerfler, S.; Althues, H.; Fujiki, S.; Shiratsuchi, T.; Tsujimura, T.; Aihara, Y.; Kaskel, S. Overcoming Binder Limitations of Sheet-Type Solid-State Cathodes Using a Solvent-Free Dry-Film Approach. *Energy Storage Mater.* **2019**, *21*, 390–398. https://doi.org/10.1016/j.ensm.2019.05.033.

(15) Kääriäinen, T.; Cameron, D.; Kääriäinen, M.; Sherman, A. Atomic Layer Deposition. Atomic layer deposition: principles, characteristics, and nanotechnology applications. *John Wiley & Sons.* **2023**. https://doi.org/10.1002/9781118747407.

(16) Kim, S.; Kang, B.; Lee, M.; Lee, S. G.; Cho, K.; Yang, H.; Park, Y. D. Sequential Solvent Casting for Improving the Structural Ordering and Electrical Characteristics of Polythiophene Thin Films. *RSC Adv.* **2014**, *4* (77), 41159–41163. https://doi.org/10.1039/c4ra06311b.

(17) Kumari, N.; Pandey, M.; Syafutra, H.; Nagamatsu, S.; Nakamura, M.; Pandey, S. S. Solvent-Assisted Friction Transfer Method for Fabricating Large-Area Thin Films of Semiconducting Polymers with Edge-On Oriented Extended Backbones. *ACS Appl. Mater. Interfaces* **2020**, *12* (49), 55033–55043. https://doi.org/10.1021/acsami.0c14874.

(18) Verdier, N.; Foran, G.; Lepage, D.; Prébé, A.; Aymé-Perrot, D.; Dollé, M. Challenges in Solvent-Free Methods for Manufacturing Electrodes and Electrolytes for Lithium-Based Batteries. *Polymers* **2021**, *13* (3), 323. https://doi.org/10.3390/polym13030323.

(19) Jiang, T.; He, P.; Wang, G.; Shen, Y.; Nan, C.; Fan, L. Solvent-Free Synthesis of Thin, Flexible, Nonflammable Garnet-Based Composite Solid Electrolyte for All-Solid-State Lithium Batteries. *Adv. Energy Mater.* **2020**, *10* (12), 1903376. https://doi.org/10.1002/aenm.201903376.

(20) Lee, D. J.; Jang, J.; Lee, J.; Wu, J.; Chen, Y.; Holoubek, J.; Yu, K.; Ham, S.; Jeon, Y.; Kim, T.; Lee, J. B.; Song, M.; Meng, Y. S.; Chen, Z. Physio-Electrochemically Durable Dry-Processed Solid-State Electrolyte Films for All-Solid-State Batteries. *Adv. Funct. Mater.* **2023**. https://doi.org/10.1002/adfm.202301341.

(21) Zhang, Z.; Wu, L.; Zhou, D.; Weng, W.; Yao, X. Flexible Sulfide Electrolyte Thin Membrane with Ultrahigh Ionic Conductivity for All-Solid-State Lithium Batteries. *Nano Lett.* **2021**, *21* (12), 5233–5239. https://doi.org/10.1021/acs.nanolett.1c01344.

(22) He, C.; Gao, C.; Zhang, J.; Li, X.; Zhou, T.; Kang, S.; Tan, L.; Jiao, Q.; Lin, C. Air-stable, Flexible Na3SbS4 Thin Membrane Prepared via a Dry-film Strategy. *J. Am. Ceram. Soc.* **2024**, *107* (1), 188–194. https://doi.org/10.1111/jace.19404.

(23) Ryu, M.; Hong, Y.-K.; Lee, S.-Y.; Park, J. H. Ultrahigh Loading Dry-Process for Solvent-Free Lithium-Ion Battery Electrode Fabrication. *Nat. Commun.* **2023**, *14* (1), 1316. https://doi.org/10.1038/s41467-023-37009-7.

(24) Sun, S.; Myung, S.; Kim, G.; Lee, D.; Son, H.; Jang, M.; Park, E.; Son, B.; Jung, Y.-G.; Paik, U.; Song, T. Facile Ex Situ Formation of a LiF–Polymer Composite Layer as an Artificial SEI Layer on Li Metal by Simple Roll-Press Processing for Carbonate Electrolyte-Based Li Metal Batteries. *J. Mater. Chem. A* **2020**, *8* (33), 17229–17237. https://doi.org/10.1039/d0ta05372d.

(25) Jokhakar, D. A.; Puthusseri, D.; Manikandan, P.; Li, Z.; Moon, J.; Weng, H.-J.; Pol, V. G. All-Solid-State Li-Metal Batteries: Role of Blending PTFE with PEO and LiTFSI Salt as a Composite Electrolyte with Enhanced Thermal Stability. *Sustain. Energy Fuels* **2020**, *4* (5), 2229–2235. https://doi.org/10.1039/d0se00013b.

(26) Oh, J. A. S.; Sun, J.; Goh, M.; Chua, B.; Zeng, K.; Lu, L. A Robust Solid–Solid Interface Using Sodium–Tin Alloy Modified Metallic Sodium Anode Paving Way for All-Solid-State Battery. *Adv. Energy Mater.* **2021**, *11* (32), 2101228. https://doi.org/10.1002/aenm.202101228.

(27) Chandrakumar, K. R. S.; Ghanty, T. K.; Ghosh, S. K. Relationship between Ionization Potential, Polarizability, and Softness: A Case Study of Lithium and Sodium Metal Clusters. *J. Phys. Chem. A* **2004**, *108* (32), 6661–6666. https://doi.org/10.1021/jp048522e.

(28) Li, J.; Li, Y.; Zhang, S.; Liu, T.; Li, D.; Ci, L. Long Cycle Life All-Solid-State Batteries Enabled by Solvent-Free Approach for Sulfide Solid Electrolyte and Cathode Films. *Chem Eng J* **2023**, *455*, 140605. https://doi.org/10.1016/j.cej.2022.140605.

(29) Lu, P.; Liu, L.; Wang, S.; Xu, J.; Peng, J.; Yan, W.; Wang, Q.; Li, H.; Chen, L.; Wu, F. Superior All-Solid-State Batteries Enabled by a Gas-Phase-Synthesized Sulfide Electrolyte with Ultrahigh Moisture Stability and Ionic Conductivity. *Adv. Mater.* **2021**, *33* (32), 2100921. https://doi.org/10.1002/adma.202100921.

(30) Pan, D.; Zhu, K.; Zhang, Y.; Sun, L.; Hao, X. First Principles and Molecular Dynamics Simulation Investigation of Mechanical Properties of the PTFE/Graphene Composites. *Compos. Part B: Eng.* **2022**, *242*, 110050. https://doi.org/10.1016/j.compositesb.2022.110050.

(31) Yang, J.; Gao, Z.; Ferber, T.; Zhang, H.; Guhl, C.; Yang, L.; Li, Y.; Deng, Z.; Liu, P.; Cheng, C.; Che, R.; Jaegermann, W.; RenéHausbrand; Huang, Y. Guided-Formation of a Favorable Interface for Stabilizing Na Metal Solid-State Batteries. *J. Mater. Chem. A* **2020**, *8* (16), 7828–7835. https://doi.org/10.1039/d0ta01498b.

(32) Huang, A.; Liu, F.; Cui, Z.; Wang, H.; Song, X.; Geng, L.; Wang, H.; Peng, X. Novel PTFE/CNT Composite Nanofiber Membranes with Enhanced Mechanical, Crystalline, Conductive, and Dielectric Properties Fabricated by Emulsion Electrospinning and Sintering. *Compos. Sci. Technol.* **2021**, *214*, 108980. https://doi.org/10.1016/j.compscitech.2021.108980.

(33) Lindberg, B. J.; Hamrin, K.; Johansson, G.; Gelius, U.; Fahlman, A.; Nordling, C.; Siegbahn, K. Molecular Spectroscopy by Means of ESCA II. Sulfur Compounds. Correlation of Electron Binding Energy with Structure. *Phys. Scr.* **1970**, *1* (5–6), 286–298. https://doi.org/10.1088/0031-8949/1/5-6/020.

(34) Nefedov, V. I.; Salyn, Ya. V.; Leonhardt, G.; Scheibe, R. A Comparison of Different Spectrometers and Charge Corrections Used in X-Ray Photoelectron Spectroscopy. *J. Electron Spectrosc. Relat. Phenom.* **1977**, *10* (2), 121–124. https://doi.org/10.1016/0368-2048(77)85010-x.

(35) Wu, E. A.; Kompella, C. S.; Zhu, Z.; Lee, J. Z.; Lee, S. C.; Chu, I.-H.; Nguyen, H.; Ong, S. P.; Banerjee, A.; Meng, Y. S. New Insights into the Interphase between the Na Metal Anode and Sulfide Solid-State Electrolytes: A Joint Experimental and Computational Study. *ACS Appl. Mater. Interfaces* **2018**, *10* (12), 10076–10086. https://doi.org/10.1021/acsami.7b19037.

(36) Tang, H.; Deng, Z.; Lin, Z.; Wang, Z.; Chu, I.-H.; Chen, C.; Zhu, Z.; Zheng, C.; Ong, S. P. Probing Solid–Solid Interfacial Reactions in All-Solid-State Sodium-Ion Batteries with First-Principles Calculations. *Chem. Mater.* **2018**, *30* (1), 163–173. https://doi.org/10.1021/acs.chemmater.7b04096.

(37) Wu, E. A.; Banerjee, S.; Tang, H.; Richardson, P. M.; Doux, J.-M.; Qi, J.; Zhu, Z.; Grenier, A.; Li, Y.; Zhao, E.; Deysher, G.; Sebti, E.; Nguyen, H.; Stephens, R.; Verbist, G.; Chapman, K. W.; Clément, R. J.; Banerjee, A.; Meng, Y. S.; Ong, S. P. A Stable Cathode-Solid Electrolyte Composite for High-Voltage, Long-Cycle-Life Solid-State Sodium-Ion Batteries. *Nat. Commun.* **2021**, *12* (1), 1256. https://doi.org/10.1038/s41467-021-21488-7.

(38) Srout, M.; Carboni, M.; Gonzalez, J.; Trabesinger, S. Insights into the Importance of Native Passivation Layer and Interface Reactivity of Metallic Lithium by Electrochemical

Impedance Spectroscopy. *Small* **2023**, *19* (7), e2206252. https://doi.org/10.1002/smll.202206252.

(39) Jiang, T.; He, P.; Liang, Y.; Fan, L.-Z. All-Dry Synthesis of Self-Supporting Thin Li10GeP2S12 Membrane and Interface Engineering for Solid State Lithium Metal Batteries. *Chem. Eng. J.* **2021**, *421*, 129965. https://doi.org/10.1016/j.cej.2021.129965.

(40) Ahmed, S.; Nelson, P. A.; Dees, D. W. Study of a Dry Room in a Battery Manufacturing Plant Using a Process Model. *J. Power Sources* **2016**, *326*, 490–497. https://doi.org/10.1016/j.jpowsour.2016.06.107.

(41) Nakano, T.; Kimura, T.; Sakuda, A.; Tatsumisago, M.; Hayashi, A. Characterizing the Structural Change of Na3PS4 Solid Electrolytes in a Humid N2 Atmosphere. *J. Phys. Chem. C* **2022**, *126* (17), 7383–7389. https://doi.org/10.1021/acs.jpcc.2c00421.

(42) Lazar, M.; Kmiec, S.; Joyce, A.; Martin, S. W. Investigations into Reactions between Sodium Metal and Na3PS4–x O x Solid-State Electrolytes: Enhanced Stability of the Na3PS3O Solid-State Electrolyte. *ACS Appl. Energy Mater.* **2020**, *3* (12), 11559–11569. https://doi.org/10.1021/acsaem.0c00914.

(43) Chi, X.; Zhang, Y.; Hao, F.; Kmiec, S.; Dong, H.; Xu, R.; Zhao, K.; Ai, Q.; Terlier, T.; Wang, L.; Zhao, L.; Guo, L.; Lou, J.; Xin, H. L.; Martin, S. W.; Yao, Y. An Electrochemically Stable Homogeneous Glassy Electrolyte Formed at Room Temperature for All-Solid-State Sodium Batteries. *Nat. Commun.* **2022**, *13* (1), 2854. https://doi.org/10.1038/s41467-022-30517-y.

(44) Lau, J.; DeBlock, R. H.; Butts, D. M.; Ashby, D. S.; Choi, C. S.; Dunn, B. S. Sulfide Solid Electrolytes for Lithium Battery Applications. *Adv. Energy Mater.* **2018**, *8* (27), 1800933. https://doi.org/10.1002/aenm.201800933.